ACS OMEGA

Open Access

http://pubs.acs.org/journal/acsodf

Article

Characterizing Dynamic Contact Angle during Gas−Liquid Imbibition in Microchannels by Lattice Boltzmann Method Modeling

Xuefeng Yang,* Cheng Chang, Majia Zheng, Xingchen Wang, Yizhao Chen, Weiyang Xie, Haoran Hu, and Qiuyang Cheng

Cite This: *ACS Omega* 2025, 10, 3116−3127

Read Online

ACCESS | Metrics & More | Article Recommendations

ABSTRACT: Spontaneous imbibition in microchannels is a critical phenomenon in various industrial applications, such as enhanced oil recovery and microfluidic systems. One of the key factors influencing the imbibition process is the dynamic wetting effect, which governs the interaction between the liquid and solid surfaces. This paper improves the original pseudopotential model for interfluid forces by coupling it with the Peng−Robinson equation of state. The model's accuracy is verified through thermodynamic consistency checks, simulations of gas−liquid interfacial tensions, and testing of static equilibrium contact angles. Following model validation, we use it to simulate spontaneous gas−liquid imbibition in microchannels and investigate dynamic contact angle evolution during the process. The results demonstrate that (1) as the microchannel width increases, inertia forces become more significant during the initial imbibition stages, leading to a greater difference between the dynamic and static contact angles. (2) A decrease in fluid−solid interaction strength results in a larger gap between dynamic and static contact angles. (3) Higher interfacial tension strengthens the capillary forces, accelerating the imbibition rate and enlarging the difference between the dynamic and static contact angles. Furthermore, the dynamic contact angle data obtained from our simulations can be used to correct the traditional Lucas−Washburn equation. The corrected equation predicts imbibition distances that closely match the simulation results.

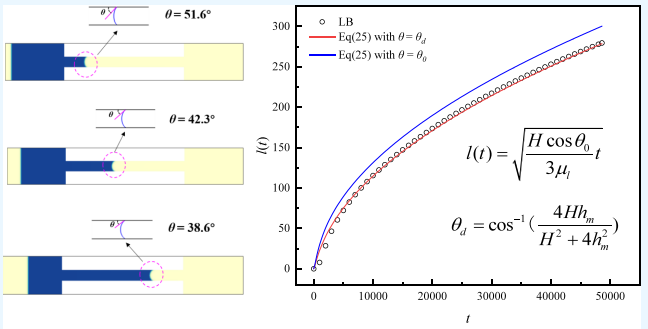

Modeling Gas-liquid imbibition by considering dynamic contact angles

INTRODUCTION

The phenomenon of spontaneous imbibition (capillary rise) refers to the process in which a wetting-phase fluid spontaneously enters a capillary tube to displace a non-wetting-phase fluid, relying only on capillary pressure.[1,2] According to different fluid phases, imbibition phenomena can be categorized into gas−liquid imbibition phenomena and liquid−liquid imbibition phenomena, among which the spontaneous gas−liquid imbibition process in microchannels is of great research significance in many fields, such as the imbibition and displacement of fracturing fluids in unconventional reservoirs,[3−5] the geologic burial of CO_2,[6,7] and the aqueous-phase transport in underground gas storage reservoirs.[8] The shape and position of the gas−liquid phase surface in the imbibition process are one of the important parameters to quantify the imbibition process. In order to characterize the relationship between the position of the phase surface and the change of the time, Lucas−Washburn established the classical theory of circular tube imbibition based on Poiseuille's law of flow (LW equation), which considers that the height of rise of the curved liquid surface is directly proportional to the square root of the time.[9,10] At the macroscopic scale, the LW equation is basically in agreement with the experimental results, but at the micro- and nanoscale, the fluid viscosity, contact angle, and other parameters are not constants during the flow process but are variables related to the thickness of the electric double layer, the flow velocity, and so on,[11,12] which will result in the height of the rise of the curved liquid level predicted by the LW equation at the micro- and nanoscale is higher than that of the experimental data.[13,14] Among the aforementioned micro-scale effects, the dynamic contact angle is considered to be the most important factor leading to a higher height of rise of the curved liquid level than the experimental data.[15]

In order to evaluate the effect of dynamic contact angle on spontaneous imbibition, researchers have combined experiment and theory to conduct a large number of studies on the dynamic wetting effect in the imbibition process, Siebold et

Received: November 14, 2024
Revised: January 2, 2025
Accepted: January 8, 2025
Published: January 17, 2025

https://doi.org/10.1021/acsomega.4c10365
ACS Omega 2025, 10, 3116−3127

al.[16] used experiments to study the imbibition process of light oil in glass capillary tubes, and the experimental results show that the dynamic contact angle in the process of imbibition is always greater than the static equilibrium contact angle and the dynamic contact angle exhibits a strong velocity correlation. Heshmati and Piri[17] measured the dynamic contact angle with time during capillary imbibition of circular and noncircular cross sections based on experimental means and corrected the LW equation using real-time data of dynamic contact angle, and the predicted results of the corrected LW equation were closer to the experimental results. Berthier et al.[18] concluded through theoretical analysis that the strength of the dynamic wetting effect is related to the capillary length, and the shorter the capillary length, the stronger the dynamic wetting effect. Kim et al.[19] used experimental means to directly measure the dynamic contact angle changes during capillary rise and applied the obtained real-time dynamic contact angle data to the LW equations, and the corrected LW equations had a good match with the experimental results. De Ruijter and Blake[20] proposed a molecular kinetic theory (MKT) to determine the dynamic contact angle during imbibition, with the central assumption that the friction of the three-phase contact line is balanced by the capillary pressure. MKT theory is widely applied to the prediction of various dynamic contact angles[21,22] but the effectiveness of its application depends on the value of the adsorption spacing of the molecules on the wall surface, which can only be obtained by fitting the experimental data. The applicability of the model will be greatly affected when the experimental data is small.

Compared with indoor experiments, the simulation method can visualize the dynamic change process of bending the liquid level during gas−liquid imbibition. The main interfacial methods for simulating spontaneous imbibition at the micro- and nanoscale include molecular dynamics simulations (MD), dissipative particle dynamics methods (DPD), and lattice Boltzmann methods (LBM).[11] Among them, the LBM has a clear physical background and particle images and is better able to compute interfacial dynamics in two-phase flows.[23,24] At the same time, the LBM can take into account microscale effects such as dynamic contact angle, inertia effects, and entrance effects that cannot be included in the traditional LW equations.[25] Based on the above two advantages, many scholars have used LBM to simulate the dynamic wetting effect in the two-phase imbibition process. Raiskinmäki et al.[26] simulated the capillary rise process for a circular cross section using the original pseudopotential LBM model and gave the relationship between the dynamic contact angle and the static contact angle and the number of capillary tubes, but there was a nonphysical case where the cosine of the dynamic contact angle was greater than 1 during the simulation. Wolf et al.[27] simulated the capillary rise process inside a flat plate based on the original pseudopotential LBM model, proposed a real-time calculation method for the dynamic contact angle, and gave the dynamic contact angle versus the number of capillaries. Lu et al.[28] simulated the dynamic capillary rise process based on the original pseudopotential LBM model and concluded that the dynamic contact angle first gradually decreases with simulation time and then gradually converges to the static contact angle. Wang et al.[29] coupled the Carnahan−Starling equation of state into a pseudopotential LBM model to simulate the dynamic imbibition process in capillary tubes with circular, rectangular, and triangular cross sections, and the results showed that the dynamic contact angle decreases with time and tends to the static equilibrium contact angle, and at the same time, the dynamic wetting effect is the weakest in capillary tubes with circular cross sections.

However, the original pseudopotential LBM model has more limitations, such as the presence of spurious velocities at the interface, thermodynamic inconsistency, and the surface tension cannot be adjusted independently,[30] which will have a greater impact on the simulation of the imbibition process. In order to overcome the various limitations in the original pseudopotential model, this paper improves the fluid−fluid force format as well as the fluid−solid force format to reduce the spurious velocities on the basis of the original pseudopotential model, couples the Peng−Robinson (PR) equations of state to improve the thermodynamic consistency of the model, and establishes a multiphase LBM simulation method with adjustable interfacial tension. Based on the established LBM, we simulate the dynamic wetting effect during spontaneous gas−liquid imbibition in microchannels, capture the real-time change of the dynamic contact angle, and focus on analyzing the effects of microchannel width, interfacial tension, and the strength of fluid−solid interaction on the dynamic contact angle in the process of gas−liquid imbibition, and the results of this paper provide theoretical and simulation bases for an in-depth understanding of the influence of the dynamic wetting effect on the gas−liquid imbibition.

1. PSEUDOPOTENTIAL MODEL

1.1. Multirelaxation MRT-LB Collision Operator.

Compared to the classical single-relaxation BGK collision operator, the multirelaxation MRT-LB collision operator has better numerical stability in simulating high density ratios and high Reynolds numbers, and the multirelaxation MRT-LB model collision process can be expressed as[31]

$$f_i(x + \mathbf{e}_i\Delta t, t + \Delta t) - f_i(x, t) = -(\mathbf{M}^{-1}\mathbf{\Lambda}\mathbf{M})_{ij}(f_j(x, t) - f_j^{eq}(x, t)) + \boldsymbol{F}_i(x, t) \quad (1)$$

In the formula, $f_i(x,t)$ is the density distribution function in the i direction, Δx and Δt denote the grid step and time step, respectively, $\boldsymbol{F}_i(x,t)$ represents the external force term, and e_i is the discrete velocity in each direction, which for the D2Q9 model used in this paper can be expressed as

$$\mathbf{e}_i = \begin{cases} 0i = 0 \\ \left(\cos\left[\frac{(i-1)\pi}{2}\right], \sin\left[\frac{(i-1)\pi}{2}\right]\right)i = 1 \sim 4 \\ \sqrt{2}\left(\cos\left[\frac{(i-5)\pi}{2} + \frac{\pi}{4}\right], \sin\left[\frac{(i-5)\pi}{2} + \frac{\pi}{4}\right]\right)i \\ = 5 \sim 8 \end{cases} \quad (2)$$

$\mathbf{M}$ is the orthogonal transformation matrix, $\mathbf{S}$ is the diagonal matrix, and $\mathbf{M}^{-1}$ is the inverse matrix of $\mathbf{M}$. The transformation matrix $\mathbf{M}$ can be written as

https://doi.org/10.1021/acsomega.4c10365
ACS Omega 2025, 10, 3116−3127

$$\mathbf{M} = \begin{bmatrix} 1 & 1 & 1 & 1 & 1 & 1 & 1 & 1 & 1 \\ -4 & -1 & -1 & -1 & -1 & 2 & 2 & 2 & 2 \\ 4 & -2 & -2 & -2 & -2 & 1 & 1 & 1 & 1 \\ 0 & 1 & 0 & -1 & 0 & 1 & -1 & -1 & 1 \\ 0 & -2 & 0 & 2 & 0 & 1 & -1 & -1 & 1 \\ 0 & 0 & 1 & 0 & -1 & 1 & 1 & -1 & -1 \\ 0 & 0 & -2 & 0 & 2 & 1 & 1 & -1 & -1 \\ 0 & 1 & -1 & 1 & -1 & 0 & 0 & 0 & 0 \\ 0 & 0 & 0 & 0 & 0 & 1 & -1 & 1 & -1 \end{bmatrix} \tag{3}$$

The density distribution function and the equilibrium density distribution function can be transformed into the moment space by the transformation matrix **M**, which can be expressed as

$$\boldsymbol{m} = \mathbf{M}f_i = (\rho, e, \varepsilon, j_x, q_x, j_y, q_y, p_{xx}, p_{xy})^T \tag{4}$$

$$\begin{aligned} \mathbf{m}^{eq} &= \mathbf{M}f_i^{eq} \\ &= \rho(1, -2 + 3|\boldsymbol{u}|^2, 1 - 3|\boldsymbol{u}|^2, u_x, -u_x, u_y, -u_y, u_x^2 \\ &\quad - u_y^2, u_x u_y)^T \end{aligned} \tag{5}$$

where ρ is the macroscopic density of the fluid, u_x and u_y are the x and y direction velocity components, respectively, and the macroscopic velocity $|\boldsymbol{u}|^2 = (\boldsymbol{u_x})^2 + (\boldsymbol{u_y})^2$, where the macroscopic density ρ and velocity $\boldsymbol{u}$ are calculated as follows.

$$\rho = \sum_i f_i, \ \boldsymbol{u} = \sum_i e_i f_i / \rho \tag{6}$$

The diagonal matrix **S** consists of nine relaxation times and can be written as

$$\mathbf{S} = \mathrm{diag}(\tau_\rho^{-1}, \tau_e^{-1}, \tau_\zeta^{-1}, \tau_j^{-1}, \tau_q^{-1}, \tau_j^{-1}, \tau_q^{-1}, \tau_v^{-1}, \tau_v^{-1}) \tag{7}$$

where τ_v is related to the kinematic viscosity, $\mu = \rho(\tau_v - 0.5)\Delta t/3$, τ_e is related to the bulk-phase viscosity, and $\boldsymbol{\tau_\rho}$ and $\boldsymbol{\tau_j}$ are generally taken as 1.0.

1.2. Interfluid and Fluid−Solid Forces. The force between fluid particles in the original pseudopotential model can be expressed as[32]

$$\boldsymbol{F}_{\mathrm{int}}(x, t) = -G\psi(x, t)c_s^2 \sum_i w(|e_i|^2)\psi(x + e_i\Delta t, t)e_i \tag{8}$$

where G is the parameter controlling the strength of the interaction between the fluids, $w(|e_i|^2)$ is the weighting coefficient, for the D2Q9 model, $|e_i|^2 = 1$, $w(|e_i|^2) = 1/3$, and $|e_i|^2 = 2$, $w(|e_i|^2) = 1/12$. ψ is the effective mass, which is also known as the "pseudopotential", and is defined as the effective mass ψ by Shan and Chen. They defined a method for calculating the effective mass ψ, which can be expressed as[32]

$$\psi = \rho_0[1 - \exp(-\rho/\rho_0)] \tag{9}$$

where $\rho_0 = 1$ is the reference density. However, it is shown that the original pseudopotential calculation method will introduce serious thermodynamic inconsistencies and large spurious velocities at the two-phase interface, which will limit the maximum density ratio and viscosity ratio of the simulation. For this reason, in this paper, we adopt the force format proposed by Gong et al.[33] to reduce spurious velocities and improve thermodynamic consistency, which can be expressed as follows

$$\boldsymbol{F}_{\mathrm{int}}(x, t) = -\beta G\psi\nabla\psi(x) - \frac{1-\beta}{2}G\nabla^2\psi(x) \tag{10}$$

where β is a tuning parameter; by adjusting the value of β, we can achieve better thermodynamic coherence. This also helps to reduce the spurious velocity at the interface between the two phases. Further considering all the nodes in the first layer as well as the four nodes in the second layer, eq 10 can be further extended as[34]

$$\begin{aligned} \boldsymbol{F}_x = &-\beta g\psi_{i,j} \\ &c_s^2\left\{\begin{array}{l} \gamma_1\left[\psi_{i+1,j} - \psi_{i-1,j}\right] + \gamma_2\left[\psi_{i+1,j+1} - \psi_{i-1,j+1}\right. \\ \left. + \psi_{i+1,j-1} - \psi_{i-1,j-1}\right] + 2\gamma_4\left[\psi_{i+2,j} - \psi_{i-2,j}\right] \end{array}\right\} \\ &-\frac{1-\beta}{2}g \\ &c_s^2\left\{\begin{array}{l} \gamma_1\left[\psi_{i+1,j}^2 - \psi_{i-1,j}^2\right] + \gamma_2\left[\psi_{i+1,j+1}^2 - \psi_{i-1,j+1}^2\right. \\ \left. + \psi_{i+1,j-1}^2 - \psi_{i-1,j-1}^2\right] + 2\gamma_4\left[\psi_{i+2,j}^2 - \psi_{i-2,j}^2\right] \end{array}\right\} \end{aligned} \tag{11}$$

$$\begin{aligned} \boldsymbol{F}_y = &-\beta g\psi_{i,j} \\ &c_s^2\left\{\begin{array}{l} \gamma_1\left[\psi_{i,j+1} - \psi_{i,j-1}\right] + \gamma_2\left[\psi_{i+1,j+1} - \psi_{i+1,j-1}\right. \\ \left. + \psi_{i-1,j+1} - \psi_{i-1,j-1}\right] + 2\gamma_4\left[\psi_{i,j+2} - \psi_{i,j-2}\right] \end{array}\right\} \\ &-\frac{1-\beta}{2}g \\ &c_s^2\left\{\begin{array}{l} \gamma_1\left[\psi_{i,j+1}^2 - \psi_{i,j-1}^2\right] + \gamma_2\left[\psi_{i+1,j+1}^2 - \psi_{i+1,j-1}^2\right. \\ \left. + \psi_{i-1,j+1}^2 - \psi_{i-1,j-1}^2\right] + 2\gamma_4\left[\psi_{i,j+2}^2 - \psi_{i,j-2}^2\right] \end{array}\right\} \end{aligned} \tag{12}$$

where $\gamma_1 = 4/15$, $\gamma_2 = 1/10$, and $\gamma_4 = 1/120$ are the force discretization coefficients, and the above force format is called the E6 force format, which yields smaller spurious velocities and more accurate interfacial tensions compared to the E4 force format and saves a portion of the computational resources compared to the E8 force format.

The fluid−solid force is similar to the format of the force between fluids, and in this paper, we use the format of the fluid−solid force based on an improved pseudopotential, which can be expressed as[35]

$$\mathbf{F}_w(x, t) = -G_w\psi(x, t)\sum_i w_i\psi(x, t)s(x + \boldsymbol{e}_i\Delta t, t)\boldsymbol{e}_i \tag{13}$$

where G_w is a parameter to control the intensity of the fluid−solid interaction; by adjusting G_w, one can obtain different contact angles of the droplets on the wall; $s(x + e_i\Delta t, t)$ is the node judgment function, if the node is a solid node, take the value of 1 and if it is a fluid node, take the value of 0. The above format of the action force can be simulated for a larger range of contact angles.

https://doi.org/10.1021/acsomega.4c10365
ACS Omega 2025, 10, 3116−3127

1.3. Equation of State. The equation of state of the original pseudopotential model can be approximated by a Taylor expansion, which can be expressed as

$$P = \rho c_s^2 + \frac{G c_s^2}{2}\psi^2 \tag{14}$$

where P is the nonideal gas pressure. However, there are major limitations in using the above equation of state format, e.g., thermodynamic inconsistency, presence of spurious velocities at the interfaces, etc. For this reason, Yuan and Schaefer[36] proposed to couple the real gas equation of state into the equation of state of the original pseudopotential model, which greatly improves the thermodynamic consistency. In this article, the Peng–Robinson (PR) equation of state is used to improve the density ratio and numerical stability of the simulation, and the PR equation of state can be expressed as follows.

$$P_{\mathrm{EOS}} = \frac{\rho RT}{1 - b\rho} - \frac{a\alpha(T)\rho^2}{1 + 2b\rho - b^2\rho^2} \tag{15}$$

where P_{EOS} is the pressure of the actual fluid, R is the gas constant, T is the temperature of the system, ρ is the density of the actual fluid, $a = 0.45724(RT_c)^2/P_c$, $b = 0.0778RT_c/P_c$ is the critical parameter, $\alpha(T) = [1 + (0.37464 + 1.54226\omega - 0.26992\omega^2)(1 - \sqrt{\mathrm{Tr}})]$, $\mathrm{Tr} = T/T_c$, and ω is the eccentricity factor, $\omega = 0.344$ for water and $\omega = 0.011$ for methane. Further, Yuan and Schaefer[36] gave the critical parameters $a = 2/49$, $b = 2/21$, and $R = 1$ in the pseudopotential model, based on which the critical temperature $T_c = 0.0729$, the critical pressure $P_c = 0.0596$, and the critical density $\rho_c = 2.657$ can be obtained. After adopting the above equations of state, the computation of pseudopotential ψ can be expressed as

$$\psi = \sqrt{\frac{2\left(\frac{\rho RT}{1 - b\rho} - \frac{a\alpha(T)\rho^2}{1 + 2b\rho - b^2\rho^2} - \rho c_s^2\right)}{G c_s^2}} \tag{16}$$

It is worth mentioning that when eq 16 is used to calculate the pseudopotential, the value of G does not have physical significance but only serves as a guarantee that the sign inside the root sign is positive, and for this reason, $G = -1$ is taken in the simulations of this paper. Meanwhile, in order to more conveniently represent the temperatures and pressures, the contrasting temperatures $T_r = T/T_c$, the contrasting pressures $P_r = P/P_c$, and the contrasting densities $\rho_r = \rho/\rho_c$ are defined.

After adding the fluid force and the fluid–solid force, this paper adopts the exact differential (EDM) format proposed by Kupershtokh et al.[37] to add the external forces to the collision operator, and the multirelaxation MRT-EDM format can be represented as

$$\boldsymbol{F}_i(x, t) = \mathbf{M}^{-1}[\boldsymbol{m}_i^{eq}(\rho, \boldsymbol{u} + \boldsymbol{F}_{\mathrm{total}}\Delta t/\rho) - \boldsymbol{m}_i^{eq}(\rho, \boldsymbol{u})] \tag{17}$$

where $F_{\mathrm{total}}=F_{int} + F_w$ represents the combined force between the fluid and the fluid–solid force.

2. MODEL VALIDATION

2.1. Verification of Thermodynamic Consistency. Thermodynamic inconsistency has been one of the major problems in pseudopotential modeling, which can be related to accurate gas–liquid density ratios and the magnitude of interfacial tension. For this reason, this paper first evaluates the thermodynamic consistency of the proposed model, and it is worth noting that the capillary pressure has a certain effect on the gas–liquid density; therefore, the thermodynamic consistency is investigated by using a gas–liquid distribution model with a flat interface and compared with the theoretical Maxwell distribution curve. A 31 × 201 lattice space is established, and the following density initialization method is adopted[38]

$$\rho(y) = \rho_v + \frac{\rho_l - \rho_v}{2}\left|\tanh\left[\frac{2(y - 50)}{W}\right] - \tanh\left[\frac{2(y - 150)}{W}\right]\right| \tag{18}$$

where W is the width of the phase interface, typically 2–5 lattice lu, and ρ_v and ρ_l are Maxwell's theoretical density magnitudes for the gas and liquid phases, respectively. After adopting the above density initialization method, the liquid phase is at the position of $50 \le y \le 150$, and the other positions are in the gas phase, and the gas–liquid interface is straight, and the effect of the capillary pressure can be neglected. Further, in this paper, the magnitude of gas–liquid coexistence density is simulated for $\beta = 1.16$, $\beta = 1.25$, and $\beta = 1.35$ and compared with Maxwell's theory of gas–liquid coexistence density. As shown in Figure 1, at $\beta = 1.25$, the LB

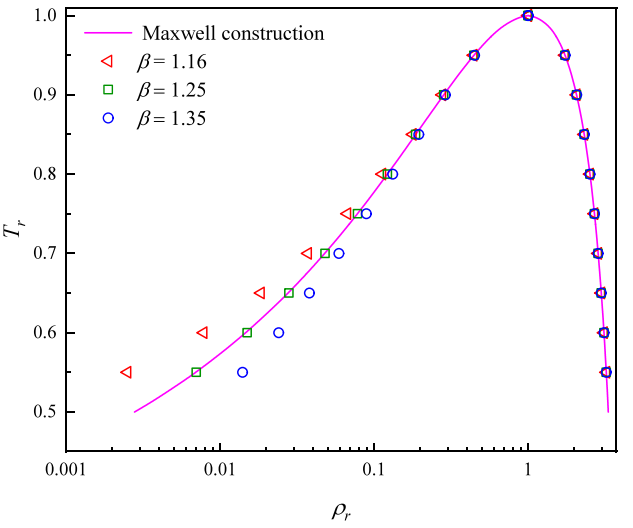

Figure 1. Thermodynamic consistency verification.

model in this paper is basically consistent with the gas–liquid coexistence density obtained from Maxwell's theory; accordingly, the next simulations in this paper all use $\beta = 1.25$.

2.2. Verification of Interface Tension. The interfacial tension is calculated by simulating a static circular droplet, and a 151 × 151 lattice space is established. The density initialization method of static droplets in the lattice space is adopted from the density initialization method proposed by Huang et al.,[39] which can be written as

$$\rho(x, y) = \frac{\rho_L + \rho_V}{2} - \frac{\rho_L - \rho_V}{2} \cdot \tanh\left[\frac{2(\sqrt{(x - x_0)^2 + (y - y_0)^2} - R_0)}{W}\right] \tag{19}$$

https://doi.org/10.1021/acsomega.4c10365
ACS Omega 2025, 10, 3116−3127

where R_0 is the initial radius of the droplet. By variation of the initial radius, a series of relationships between the gas-hydraulic pressure difference and the radius can be established. The interfacial tension can then be calculated using the Young−Laplace equation: $\Delta P = \sigma/r$, where r is the radius of the droplet in the steady state. In order to obtain more accurate droplet diameters, this paper uses the difference method proposed by Wen et al.[40] to determine the gas−liquid interfacial position in the following format

$$\boldsymbol{x}_p = \boldsymbol{x}_g + \frac{\rho_m - \rho(\boldsymbol{x}_g)}{\rho(\boldsymbol{x}_l) - \rho(\boldsymbol{x}_g)}\boldsymbol{n} \tag{20}$$

where x_p denotes the actual position of the partition line, x_g and x_l are the positions of the neighboring gas-phase and liquid-phase lattice nodes, respectively, $\rho(x_g)$ and $\rho(x_l)$ are the densities of the gas-phase and liquid-phase lattice nodes, respectively, $\rho_m = (\rho_g + \rho_l)/2$, and $\boldsymbol{n}$ denotes the direction vector. As shown in Figure 2a, the fitted curves of interfacial tension at three different temperatures are given in this paper, the fitting effect shows a good linear relationship ($R^2 > 0.999$), and the slopes of the straight lines, i.e., the interfacial tensions, are 0.428, 0.286, and 0.169. Further, in order to relate the simulation results to the actual gas−liquid interfacial tension, the unit conversion method proposed by Huang et al.[39] is used, which can be expressed as

$$\frac{\sigma_{real}/\lambda_1}{P_{c,real}} = \frac{\sigma_{LB}/\Delta x}{P_{c,LB}} \tag{21}$$

where σ_{LB} and σ_{real} denote the two-phase interfacial tension obtained by LB simulation and the actual gas−liquid interfacial tension, respectively. $P_{c,LB} = 0.0596$ and $P_{c,real} = 4.61$ MPa denote the critical pressure in the LB simulation and the actual critical pressure, respectively.

As shown in Figure 2b, when $\lambda_1 = 0.4$ nm, the simulation results are basically consistent with the experimental results (experimental data from the NIST database); for this reason, the grid step of the LB simulation in this paper is determined to be 0.4 nm, and the subsequent simulation parameters in this paper are all in the lattice unit (lu), unless otherwise specified.

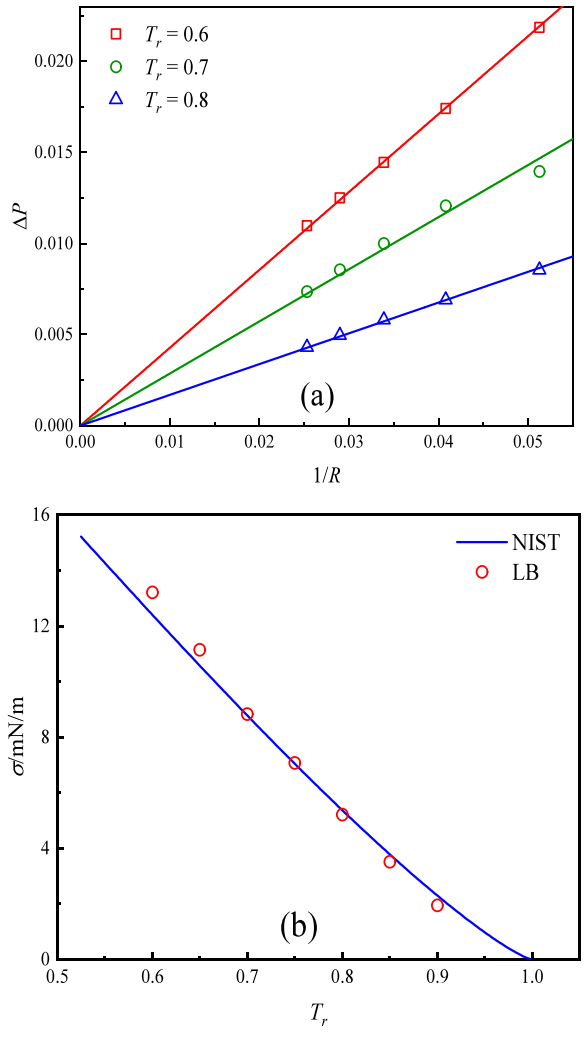

Figure 2. (a) Interfacial tension verification; (b) comparison of interfacial tension from LB simulation and NIST experimental data.

2.3. Static Equilibrium Contact Angle. In this section, fluid−solid forces are added to the consideration of interfluid forces to simulate and verify different contact angles of droplets on the wall. For a given droplet height and droplet base length, the magnitude of the droplet contact angle on the wall is calculated as follows[41]

$$r = \frac{4\xi_2^2 + \xi_1^2}{8\xi_2} \tag{22}$$

$$\theta = \begin{cases} \arcsin\left(\dfrac{\xi_1}{2r}\right), \theta \le 90^\circ \\ \pi - \arcsin\left(\dfrac{\xi_1}{2r}\right), \theta > 90^\circ \end{cases} \tag{23}$$

where θ is the contact angle of the droplet, ξ_1 is the length of the contact line between the droplet and the solid wall, and ξ_2 is the height of the droplet. In order to simulate and verify the different contact angle sizes, a 201 × 101 lattice region is established, with periodic boundaries on the left and right and bouncing boundaries on the top and bottom walls, taking $T = 0.7T_c$. In this paper, we adopt the density initialization method proposed by Li et al.,[35] which has the following format

$$\rho(x, y) = \begin{cases} \rho_l, \text{ if} (x - x_0)^2 + (y - y_0)^2 \le R_0^2 \\ \rho_v, \text{ otherwise} \end{cases} \tag{24}$$

where R_0 is the droplet initialization radius, which is taken as 15 lu in this paper. ρ_l and ρ_v are the densities of the liquid and gas phases, respectively. When $(x_0, y_0) = (100, 90)$, the simulation results are shown in Figure 3. The fluid−solid interaction strength G_w exhibits an approximately linear relationship with contact angle θ. Different sizes of static equilibrium contact angles can be realized by varying G_w.

3. RESULTS AND DISCUSSION

3.1. Effect of Dynamic Contact Angle. Most of the previous indoor imbibition experiments as well as simulations have been carried out on circular tubes, and there are fewer studies on imbibition through slit pores, but it has been shown that the dynamic wetting effect of circular tubes is weak.[42] For this reason, in this paper, we take the microchannel of slit pore type as the object of study; as shown in Figure 4, the kinetic equations of incompressible fluid in microchannel when it is undergoing imbibition in the horizontal direction are[43]

https://doi.org/10.1021/acsomega.4c10365
ACS Omega 2025, 10, 3116−3127

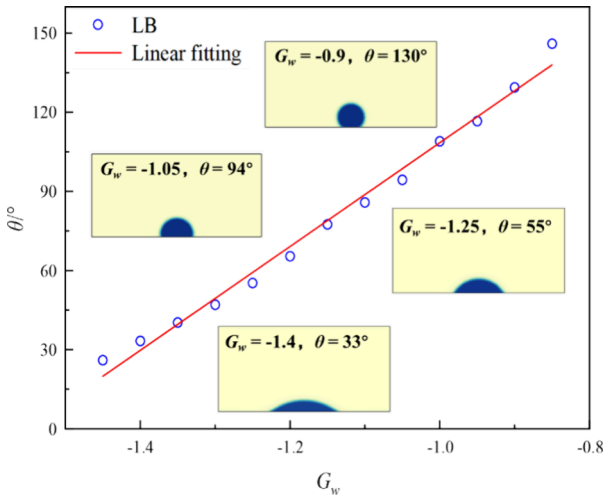

Figure 3. Verification for static equilibrium wetting angle.

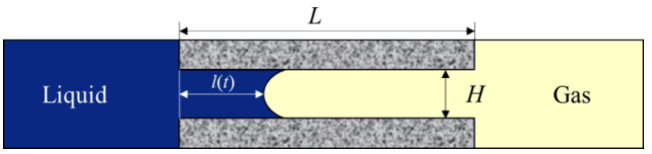

Figure 4. Schematic diagram of the gas−liquid imbibition process.

$$2\frac{\sigma\cos\theta}{H} - [\rho_l l + (L-l)\rho_v]\frac{d^2 l}{dt^2} - [\rho_l l + (L-l)\rho_v](\frac{dl}{dt})^2 - \frac{12}{H^2}\frac{dl}{dt}[\mu_l l + (L-l)\mu_v] = 0 \quad (25)$$

where L is the length of the microchannel, l is the height of the imbibition; H is the width of the capillary; μ_l and μ_v are the dynamic viscosity of the liquid and gas phases, respectively; θ is the contact angle; $\theta = \theta_0$ is the static equilibrium contact angle if the dynamic wetting effect is neglected in the calculation process. Meanwhile, the items of eq 25 (from left to right) represent the capillary force, inertia force, and viscous force, respectively, in which the capillary force is the main driving force in the process of imbibition, the viscous force is the main resistance in the process of imbibition, and the inertia force mainly exists in the early stage of imbibition in the unsteady flow of liquid.

Considering that eq 25 is a typical second-order constant coefficient nonchiral linear differential equation, it is difficult to determine the general solution of such problems directly using mathematical methods. If the effects of gas-phase viscosity, inertial forces, and dynamic wetting effects are not taken into account, eq 25 can be simplified to yield the following analytical solution[44]

$$l(t) = \sqrt{\frac{H\cos\theta_0}{3\mu_l}t} \quad (26)$$

Equation 26 is the classical Lucas−Washburn equation; however, it has been shown that neglecting the effects of gas-phase viscosity and inertial forces will overestimate the position of the curved liquid level during imbibition.[45] In order to fully consider the effects of gas-phase viscosity and inertial forces, the fourth-order explicit Runge−Kutta method is used in this paper to directly solve the numerical solution of eq 25, with reference to the literature.[27]

In order to verify the applicability of the above theoretical model, a lattice space of 601 × 101 is established, a channel with a length of 300 lu and a width of 28 lu is set at the position of 150 < x < 450, the contact angle of the channel wall is set to θ_0 = 33° with a no-slip bounce format, the rest of the boundaries are in a periodic boundary with a simulated temperature of $T = 0.7T_c$, the channel is set to be in a x < 150 position as a liquid phase (wetting phase), and the rest of the positions were set to gas phase. Figure 5 gives the spontaneous

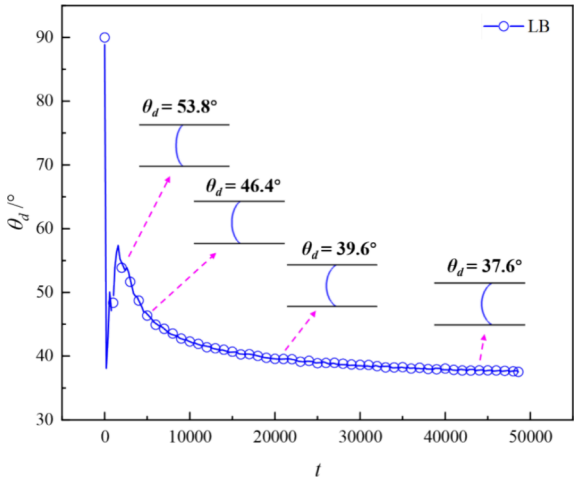

Figure 5. Evolution of dynamic wetting angle with time.

gas−liquid imbibition process in the microchannel, and it can be seen that the gas−liquid interface moves forward in the form of a curved liquid surface under the action of the capillary force; the radius of curvature of the curved liquid surface decreases gradually with time, which is due to the effect of the imbibition rate that makes the contact angle in the imbibition process change with time. In order to quantitatively evaluate the relationship between the change of dynamic contact angle with time in the process of imbibition and absorption, this paper proposes a real-time calculation of dynamic contact angle to capture the change of dynamic contact angle with time in the process of imbibition and absorption, which is denoted as

$$\theta_d = \cos^{-1}\left(\frac{4Hh_m}{H^2 + 4h_m^2}\right) \quad (27)$$

where θ_d denotes the dynamic contact angle and h_m denotes the height of the bent liquid surface (i.e., the horizontal distance between the three-phase contact point and the apex of the bent liquid surface).

Figure 6 gives the evolution of the dynamic contact angle with time in the process of imbibition and absorption. Since the interface between the two phases is flat at the initial moment (t = 0), the contact angle at the initial moment is 90° in the simulation; at the early stage of imbibition and absorption (t < 1600), due to the inertial force and the effect of the inlet effect, the dynamic contact angle first decreases and then rises rapidly; with the simulation of the time step increases, the dynamic contact angle gradually decreases and tends to the static equilibrium contact angle. As the simulation time step increases, the dynamic contact angle gradually

https://doi.org/10.1021/acsomega.4c10365
ACS Omega 2025, 10, 3116−3127

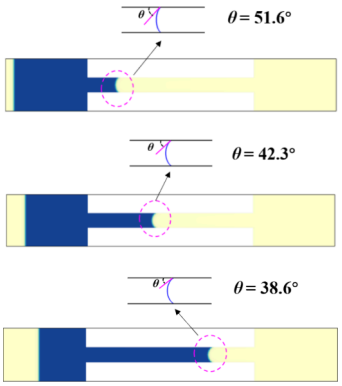

Figure 6. Simulation results of spontaneous gas−liquid imbibition at different time steps.

decreases and converges to the static equilibrium contact angle. It is worth noting that, in the whole simulation of the imbibition process, the dynamic wetting phenomenon always exists because the imbibition rate is not 0, and the dynamic contact angle is always larger than the static equilibrium contact angle. However, along with the increase of the liquid-phase imbibition distance, the viscous resistance in the imbibition process gradually increases, the imbibition rate gradually decreases, and the dynamic wetting effect will gradually weaken. When the simulation time reaches 48,000 steps, the dynamic contact angle θd =37.5° is close to the static equilibrium contact angle θ_0 =33.0°. The trend of the dynamic contact angle obtained from the simulation in this paper is consistent with the studies of Wolf et al.,[27] which indicates that that the simulation results in this paper are accurate.

Further, the imbibition length obtained from the simulation is compared with the imbibition length predicted by eq 25. As shown in Figure 7, if the dynamic contact angle change during

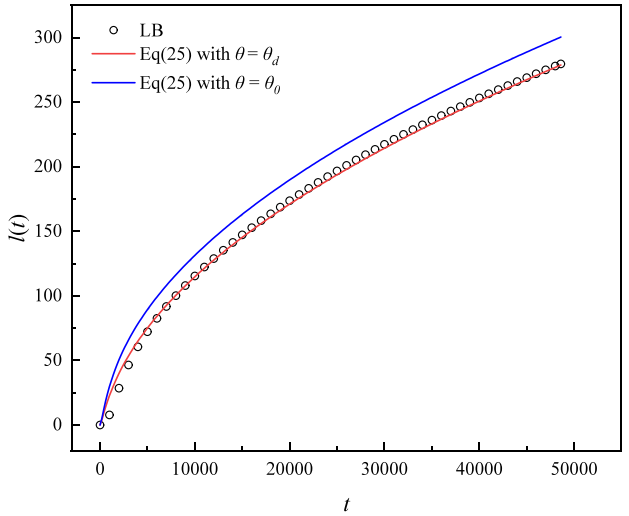

Figure 7. Comparison of the LB simulated imbibition length with theoretical results.

the imbibition process is not taken into account, there is a 7.5% deviation between the imbibition length predicted by eq 25 and the simulation result (t = 48000); based on the research,[19] the real-time dynamic contact angle data obtained from Figure 6 is applied to eq 25 for correction (i.e., replacing θ_0 with θ_d in eq 25) and solved it by the fourth-order explicit Runge−Kutta method. It can be seen that the imbibition length predicted by the LW equation after correcting for the dynamic contact angle is basically the same as the simulation results, which indicates that the dynamic contact angle is the reason for the deviation of the LW equation from the simulation results. It is shown that the dynamic contact angle is related to the moving speed of the curved liquid surface, and the capillary force $p_c = 2\sigma\cos\theta/H$ is the main driving force of the imbibition and the main factor controlling the imbibition rate, which also indicates that the factors such as the width of the microchannel, the interfacial tension, and the static contact angle will significantly affect the power of the imbibition and the imbibition rate; therefore, this paper analyzes the effect of the above factors on the dynamic contact angle by changing the factors of the width of the microchannel and the magnitude of the static contact angle, by using simulation. Therefore, this paper analyzes the influence of the above factors on the dynamic contact angle through simulation by changing the microchannel width and the static contact angle size, combined with the proposed pseudopotential LBM model.

3.2. Effect of Microchannel Width. In order to evaluate the effect of microchannel width on the dynamic contact angle, a lattice space of 601 × 101 is established in this section, microchannels with a length of 300 lu and widths of 28, 38, and 48 lu are set at the position of 150 < x < 450, and the static contact angle of the wall is set to 33°. In order to ensure that the simulation is carried out in a stable manner, the positions at x < 150 as well as x > 500 are set to be the liquid phase, other positions are set to gas phase, and the rest of the simulation parameters and boundary conditions are the same as in Section 2.1. The simulation results are listed in Figure 8.

Figure 8a compares the changes of the dynamic contact angle with time in the process of imbibition under the conditions of three different channel widths. In the initial stage of imbibition (t < 3000), the larger the width of the microchannels is, the stronger the inertial resistance is to the fluid in the pores, and the rate of imbibition decreases, so that the dynamic contact angle in the smaller the gap between the contact angle and the static contact angle is and the dynamic wettability effect is weakened. With the increase of the imbibition time, the role of inertial force is weakened, the role of viscous drag force is enhanced, and the dynamic contact angles under different channel width conditions are all gradually decreased; when the simulation time t = 30,000, the dynamic contact angles in the three kinds of microchannels are 38.5° (H = 28 lu), 40.7° (H = 38 lu), and 42.8° (H = 48 lu). It is worth noting that in Figure 8a, the effect of microchannel width on the dynamic wetting effect shows a different pattern in the early and midlate stages of imbibition, so that the curves have a "crossover". In the early stage of imbibition (t < 3000), it is mainly affected by the inertia force, and the larger the pore width is, the weaker the dynamic wetting effect is in the middle and late stages of imbibition; the dynamic contact angle is rather larger with the larger microchannel width.

The reason for this phenomenon is complex. Stroberg et al.[46] and others believe that the migration rate of the three-phase contact line at the leading edge of the gas−liquid bending interface is different from the fluid imbibition rate; the larger the pore, the slower the migration rate of the three-phase contact line is, and the larger the difference with the overall imbibition rate of the fluid, which exacerbates the dynamic wetting effect. Overall, our simulation results are consistent

https://doi.org/10.1021/acsomega.4c10365
ACS Omega 2025, 10, 3116−3127

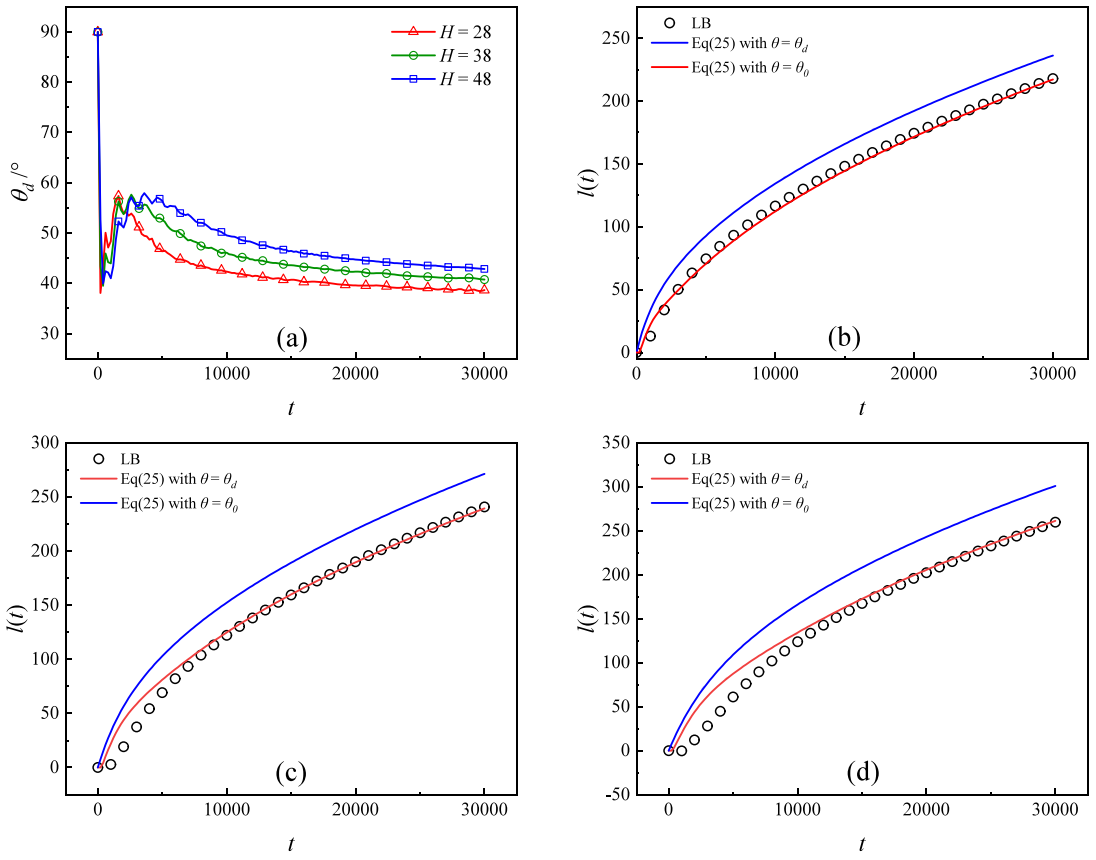

Figure 8. (a) Evolution of dynamic wetting angle with time for different microchannel widths; (b) comparison of theoretical imbibition length with LB simulation results at H = 28 lu; (c) H = 38 lu; (d) H = 48 lu.

with the molecular simulation results of Stroberg et al.,[46] i.e., the dynamic contact angle within the microchannels exhibits a strong scale dependence, and the influence of the three-phase contact line on the dynamic wetting effect during the middle and late stages of imbibition needs to be further investigated. Comparisons of the theoretical and LB simulation results of the imbibition length over time in the three different channel widths mentioned above are given in Figure 7b–d, which show that the LW equations deviate from the simulation results by 8.4%, 12.9%, and 15.8% without considering the dynamic contact angle, and the deviation increases as the channel radius increases. The method in Section 4.1 was used to correct the LW equations using the real-time dynamic contact angle data in Figure 7a, and the predicted imbibition lengths of the corrected LW equations remained essentially the same as those in the simulation results.

3.3. Influence of the Strength of Fluid–Solid Interaction. The effect of different fluid–solid interaction strengths on the dynamic contact angle during imbibition is investigated by varying the different fluid–solid interaction force parameters G_w. In order to minimize the effect of inertial action, the width of the microchannels is likewise fixed constant at 28 lu in this section. The simulation parameters are chosen as $G_w = -1.45$, $\theta = 26°$, $G_w = -1.35$, $\theta = 40°$, and $G_w = -1.25$, $\theta = 55°$, and the rest of the model parameters and boundary conditions are the same as in Section 3.1. The simulation results are listed in Figure 9.

Figure 9a gives the variation of dynamic contact angle with time for different time steps of the imbibition process, and the influence of inertia force on the dynamic contact angle in the three cases at the early stage of imbibition is basically the same. As the simulation time step increases, the dynamic contact angles of the three cases decrease, and when the simulation time t = 30000, the dynamic contact angles of the three cases are 29.5° (θ_0 = 26°), 47.1° (θ_0 = 40°), and 64.4° (θ_0 = 55°), respectively. It is observed that the static contact angle becomes larger as the strength of the fluid–solid interaction decreases, and the gap between the dynamic contact angle and the static contact angle increases in the process of imbibition. This phenomenon indicates that the weaker the strength of the fluid–solid interaction, the easier the gas–liquid bending liquid surface in the microchannel deforms and the more significant is the change of the contact angle. Further, Figure 9b–d compares the variation of the imbibition length with time obtained based on the LB simulation as well as the LW equation for different fluid–solid interaction strengths, and with the weakening of the fluid–solid interaction strengths, there is a large deviation between the LW equation and the imbibition length predicted by simulation results if the effect of the dynamic contact angle is neglected (t = 30,000). Using the same method, the LW equation is corrected by using the real-time dynamic contact angle data in Figure 9a, and it can be seen that the predictions of the LW equation after correcting the dynamic contact angle are in good agreement with the simulation results.

3.4. Effect of Interfacial Tension. Interfacial tension is likewise one of the main factors affecting the dynamics of imbibition; however, the interfacial tension in the original pseudopotential model is often related to the density ratio cannot be regulated independently (i.e., changing the surface

https://doi.org/10.1021/acsomega.4c10365
ACS Omega 2025, 10, 3116–3127

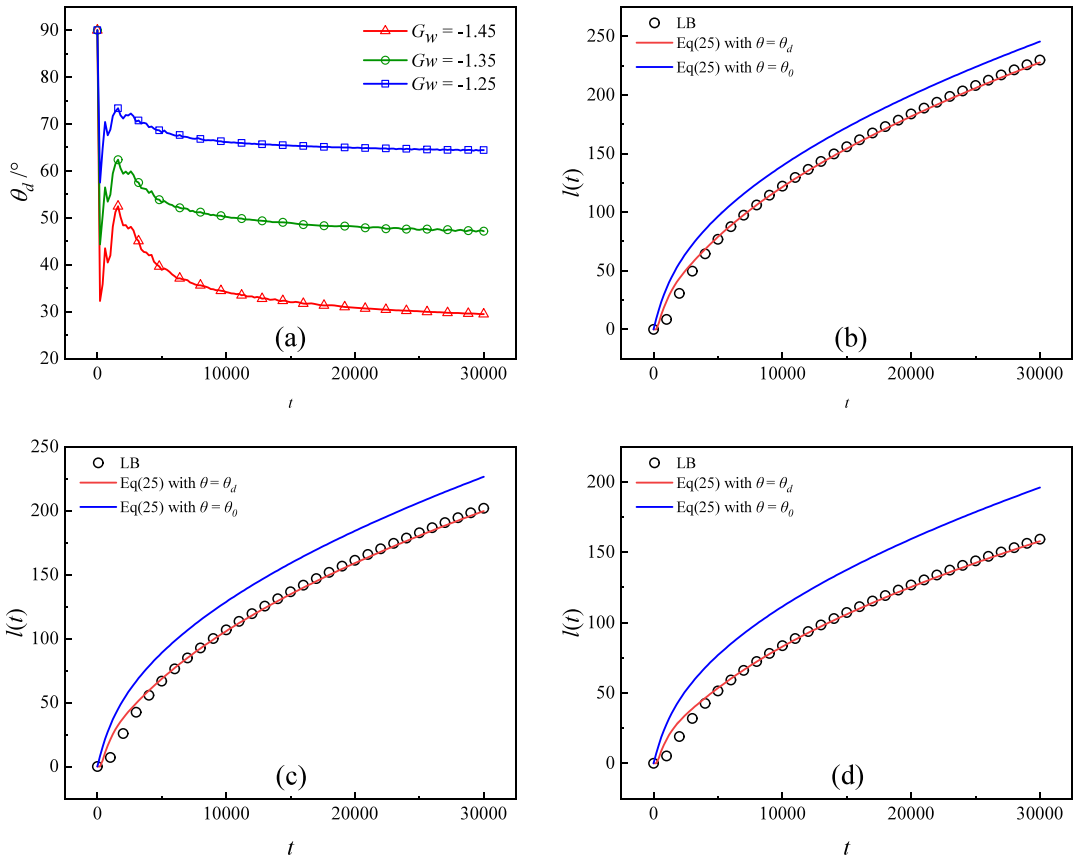

Figure 9. (a) Evolution of dynamic wetting angle with time for different G_w; (b) comparison of theoretical imbibition length with LB simulation for $G_w = -1.45$; (c) $G_w = -1.35$; (d) $G_w = -1.25$.

tension is accompanied by a concomitant change in the density ratio). In 2013, Li and Luo[47] proposed a method of regulating the surface tension, which consists of adding to the collision step in the space of moments a source term **C**.

$$\mathbf{C} = [0,\ 1.5\tau_e^{-1}(Q_{xx} + Q_{yy}),\ -1.5\tau_\zeta^{-1}(Q_{xx} + Q_{yy}),\ 0,\ 0,\ 0,\ -\tau_\nu^{-1}(Q_{xx} - Q_{yy}),\ -\tau_\nu^{-1}Q_{xy}]^{\mathrm{T}} \tag{28}$$

Q_{xx}, Q_{yy}, and Q_{xy} in eq 28 are calculated by the following equation.

$$Q = \kappa\frac{G_{11}}{2}\psi(x)\sum_{i=1} w_i[\psi_1(x + \mathbf{e}_i\Delta t) - \psi_1(x)]\mathbf{e}_i\mathbf{e}_i \tag{29}$$

where the parameter κ is used to adjust the magnitude of the surface tension; the above format allows for a wide range of surface tension adjustments, while the simulated density ratio of the two phases remains almost constant. The simulation parameters selected in this section are shown in Table 1, and it should be noted that the process of adjusting the interfacial tension and simulating the contact angle is consistent with the process of verifying the interfacial tension in Section 2.2.

Table 1. Simulation Parameters of Interfacial Tension and Contact Angle

parameter	interfacial tensions	interaction forces	contact angle
$\kappa = -0.5$	$\sigma = 0.36$	$G_w = -1.37$	$\theta = 42.6°$
$\kappa = 0.0$	$\sigma = 0.286$	$G_w = -1.33$	$\theta = 42.4°$
$\kappa = 0.5$	$\sigma = 0.229$	$G_w = -1.29$	$\theta = 42.5°$

The effect of different interfacial tensions on the dynamic contact angle during imbibition is investigated by varying different parameters κ. In order to minimize the effect of inertial effects, the width of the microchannel is likewise fixed to be unchanged at 28 lu in this section, and the rest of the model parameters and boundary conditions are the same as those in Section 4.1. The simulation results are listed in Figure 10.

Figure 10a gives the variation of dynamic contact angle with time in the process of imbibition at different time steps, and the overall evolution of the dynamic contact angle is consistent with the previous simulation results; when the simulation time is $t = 40000$, the dynamic contact angle in the three cases are 48.0°, 50.1°, and 51.9°. This indicates that with the increase of interfacial tension, the dynamic contact angle increases and leads to the increase of dynamic contact angle during the imbibition process, which is consistent with the results of MKT theory by Tian et al.[22] Further, Figure 10b–d compares the LB-based simulations as well as the LW equation for obtaining the imbibition length with time under different interfacial tension conditions, and the LW equation neglecting the effect of the dynamic contact angle shows a deviation of 12.7% from the imbibition length predicted by the simulation results (t = 40,000). Using the same method, the real-time dynamic contact angle data in Figure 10a is utilized to correct the LW equation, and the prediction results of the LW equation after correcting the dynamic contact angle are in good agreement with the simulation results

https://doi.org/10.1021/acsomega.4c10365
ACS Omega 2025, 10, 3116−3127

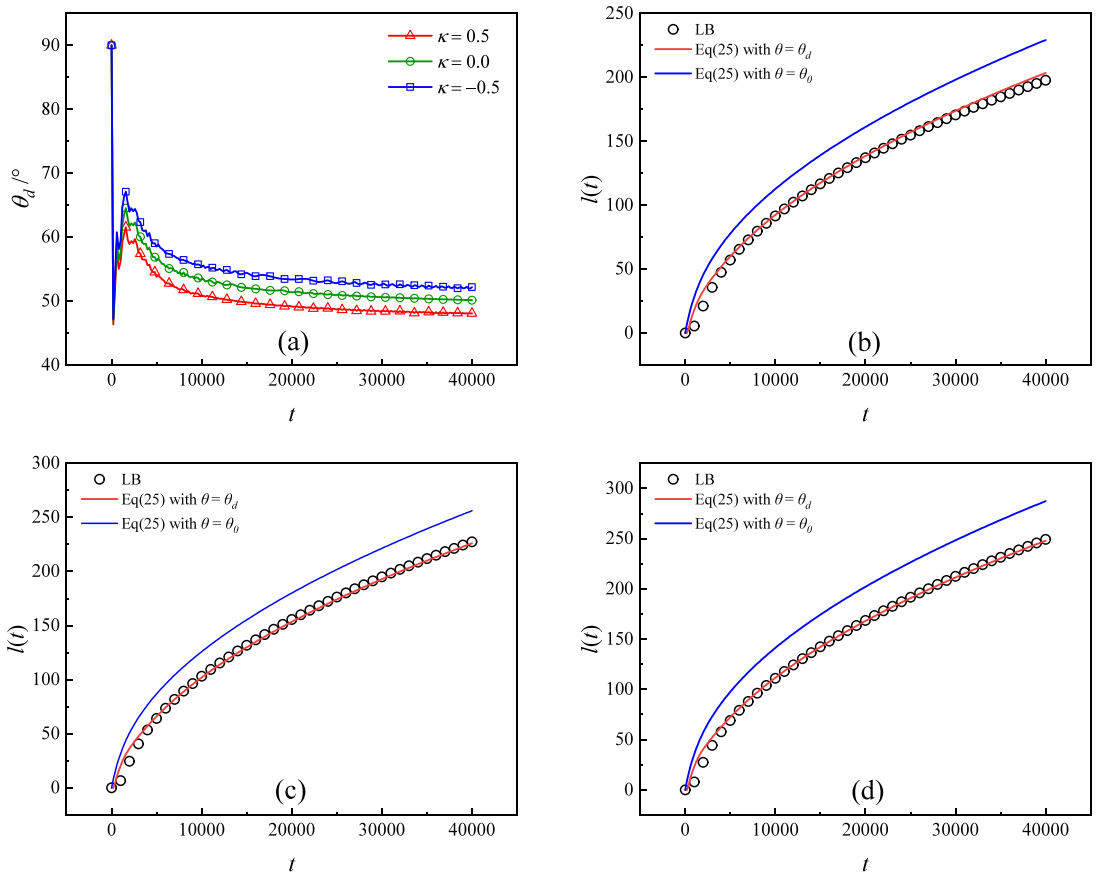

Figure 10. (a) Evolution of dynamic wetting angle with time for different interfacial tensions; (b) comparison of theoretical imbibition length with LB simulation results for κ = 0.5; (c) κ = 0.0; (d) κ = −0.5.

4. CONCLUSIONS

In this article, a microscopic gas−liquid two-phase flow simulation method is established, and the dynamic wetting angle characteristics and related influencing factors in the spontaneous imbibition process are investigated. The following conclusions are obtained.

1) Dynamic wetting effect always exists in the process of gas−liquid imbibition in the microchannel, and the dynamic wetting effect is more significant in the early stage of imbibition due to the influence of inertial force. With the increase of simulation time, the radius of curvature of gas−liquid curved liquid surface decreases gradually, and the dynamic wetting angle decreases gradually. However, due to the presence of imbibition velocity, the dynamic contact angle is always numerically larger than the static equilibrium contact angle.
2) The size of the dynamic contact angle in the imbibition process is related to the width of the microchannel, the strength of the fluid−solid interaction, and the interfacial tension. The larger width of the microchannel leads to the larger real-time dynamic contact angle in the simulated imbibition process. The weaker fluid−solid force leads to the larger difference between the real-time dynamic contact angle and the static contact angle. The larger the interfacial tension leads to the larger imbibition driving force and the larger real-time dynamic contact angle.
3) The existence of dynamic contact angle will lead to a 7.5%∼15.8% deviation of the imbibition distance predicted by the traditional LW equation. The real-time data of the dynamic contact angle obtained by LBM simulation can be directly applied to the real-time correction of LW equation, and the predicted imbibition distance of the corrected LW equation is basically consistent with the simulation results. Therefore, our simulation method provides a new basis for the characterization of the dynamic wetting mechanism of gas−liquid imbibition in nanochannels and porous media.

AUTHOR INFORMATION

Corresponding Author

Xuefeng Yang − *PetroChina Southwest Oil & Gas Field Company, Chengdu, Sichuan Province 610051, China*; orcid.org/0009-0002-8024-9019; Email: Yangxf@petrochina.com.cn

Authors

Cheng Chang − *PetroChina Southwest Oil & Gas Field Company, Chengdu, Sichuan Province 610051, China*

Majia Zheng − *PetroChina Southwest Oil & Gas Field Company, Chengdu, Sichuan Province 610051, China*

Xingchen Wang − *PetroChina Southwest Oil & Gas Field Company, Chengdu, Sichuan Province 610051, China*

Yizhao Chen − *PetroChina Southwest Oil & Gas Field Company, Chengdu, Sichuan Province 610051, China*

Weiyang Xie − *PetroChina Southwest Oil & Gas Field Company, Chengdu, Sichuan Province 610051, China*

https://doi.org/10.1021/acsomega.4c10365
ACS Omega 2025, 10, 3116−3127

Haoran Hu − *PetroChina Southwest Oil & Gas Field Company, Chengdu, Sichuan Province 610051, China*
Qiuyang Cheng − *PetroChina Southwest Oil & Gas Field Company, Chengdu, Sichuan Province 610051, China*

Complete contact information is available at: https://pubs.acs.org/10.1021/acsomega.4c10365

Notes

The authors declare no competing financial interest.

■ ACKNOWLEDGMENTS

All the authors in this paper acknowledgement technical supports by work teams from China University of Petroleum (Beijing).

■ REFERENCES

(1) Jianchao, Cai; Yu, B. Advances in studies of spontaneous imbibition in porous media [J]. *Adv. Mech.* **2012**, *42* (6), 735−754.
(2) Liu, P.; Zhao, J.; Li, Z.; Wang, H. Numerical simulation of multiphase multi-physics flow in underground reservoirs: Frontiers and challenges[J]. *Capillarity* **2024**, *12* (3), 72−79.
(3) Qin, X.; Xia, Y.; Qiao, J.; Chen, J.; Zeng, J.; Cai, J. Modeling of multiphase flow in low permeability porous media: Effect of wettability and pore structure properties[J]. *J. Rock Mech. Geotech. Eng.* **2024**, *16* (4), 1127−1139.
(4) Wang, H.; Cai, J.; Su, Y.; Jin, Z.; Wang, W.; Li, G. Imbibition behaviors in shale nanoporous media from pore-scale perspectives[J]. *Capillarity* **2023**, *9* (2), 32−44.
(5) Cai, J.; Jin, T.; Kou, J.; Zou, S.; Xiao, J.; Meng, Q. Lucas−washburn equation-based modeling of capillary-driven flow in porous systems. [J]. *Langmuir* **2021**, *37* (5), 1623−1636.
(6) Zhang, Z.; Cai, J.; Chen, F.; Li, H.; Zhang, W.; Qi, W. Progress in enhancement of CO2 absorption by nanofluids: A mini review of mechanisms and current status [J]. *Renewable energy* **2018**, *118*, 527−535.
(7) Zhou, Y.; Guan, W.; Zhao, C.; Zou, X.; He, Z.; Zhao, H. Numerical methods to simulate spontaneous imbibition in microscopic pore structures: A review[J]. *Capillarity* **2024**, *11* (1), 1−21.
(8) Yang, Y.; Horne, R. N.; Cai, J.; Yao, J. Recent advances on fluid flow in porous media using digital core analysis technology[J]. *Adv, in Geo-Energy Res,* **2023**, *9* (2), 71−75.
(9) Lucas, R. Ueber das Zeitgesetz des kapillaren Aufstiegs von Flüssigkeiten [J]. *Kolloid-Z.* **1918**, *23* (1), 15−22.
(10) Washburn, E. W. The Dynamics of Capillary Flow [J]. *Phys. Rev.* **1921**, *17* (3), 273−283.
(11) Wang, W.; Xie, Q.; Wang, H.; Su, Y.; Rezaei-Gomari, S. Pseudopotential-based multiple-relaxation-time lattice Boltzmann model for multicomponent and multiphase slip flow[J]. *Adv. Geo-Energy Res.* **2023**, *9* (2), 106−116.
(12) Cai, J.; Jiao, X.; Wang, H.; He, W.; Xia, Y. Multiphase fluid-rock interactions and flow behaviors in shale nanopores: A comprehensive review[J]. *Earth-Science Reviews* **2024**, No. 104884.
(13) Zhang, S.; Li, J.; Coelho, R. C. V.; Wu, K.; Zhu, Q.; Guo, S.; Chen, Z. Lattice Boltzmann modeling of forced imbibition dynamics in dual-wetted porous media[J]. *Int. J. Multiphase Flow* **2025**, *182*, 105035−105035.
(14) Shengting, Z.; Jing, L.; Zhu Qingyuan, W.; Keliu, C. Z.; Ziyi, W. Simulation of droplet dynamics in an inclined channel considering contact angle hysteresis using the cascade lattice Boltzmann method[J]. *Phys. Fluids* **2024**, *36* (1), No. 012130.
(15) Hamraoui, A.; Thuresson, K.; Nylander, T.; Yaminsky, V. Can a dynamic contact angle be understood in terms of a friction coefficient? [J]. *J. Colloid Interface Sci.* **2000**, *226* (2), 199−204.
(16) Siebold, A.; Nardin, M.; Schultz, J.; Walliser, A.; Oppliger, M. Effect of dynamic contact angle on capillary rise phenomena[J]. *Colloids Surf. A* **2000**, *161* (1), 81−87.
(17) Heshmati, M.; Piri, M. Experimental investigation of dynamic contact angle and capillary rise in tubes with circular and noncircular cross sections [J]. *Langmuir* **2014**, *30* (47), 14151−14162.
(18) Berthier, J.; Gosselin, D.; Delapierre, G. Spontaneous capillary flow: should a dynamic contact angle be taken into account? [J]. *Sens. Trans.* **2015**, *191* (8), 40.
(19) Kim, H.; Lim, J. H.; Lee, K.; Choi, S. Q. Direct Measurement of Contact Angle Change in Capillary Rise [J]. *Langmuir* **2020**, *36* (48), 14597−14606.
(20) De Ruijter, M. J.; Blake, T. D.; De Coninck, J. Dynamic wetting studied by molecular modeling simulations of droplet spreading[J]. *Langmuir* **1999**, *15* (22), 7836−7847.
(21) Tian, W.; Wu, K.; Chen, Z.; Lei, Z.; Gao, Y.; Chen, Z.; Liu, Y.; Hou, Y.; Zhu, Q.; Li, J. Dynamic wetting of solid-liquid-liquid system by molecular kinetic theory [J]. *J. Colloid Interface Sci.* **2020**, *579*, 470−478.
(22) Tian, W.; Wu, K.; Chen, Z.; Lai, L.; Gao, Y.; Li, J. Effect of dynamic contact angle on spontaneous capillary-liquid-liquid imbibition by molecular kinetic theory [J]. *SPE J.* **2021**, *26* (4), 2324−2339.
(23) Zhang, S.; Li, J.; Chen, Z.; Wu, K.; Zhu, Q. Investigation on spontaneous liquid−liquid imbibition in capillaries with varying axial geometries using lattice Boltzmann method[J]. *Phys. Fluids* **2023**, *35* (12), No. 122108.
(24) Sedahmed, M.; Coelho, R. C. V.; Araújo, N. A. M.; Wahba, E. M.; Warda, H. A. Study of fluid displacement in three-dimensional porous media with an improved multicomponent pseudopotential lattice Boltzmann method[J]. *Phys. Fluids* **2022**, *34* (10), No. 103303.
(25) Moradi, B.; Ghasemi, S.; Hosseini Moghadam, A.; Rasaei, M. R.; Sajjadi, M. Dynamic behavior investigation of capillary rising at various dominant forces using free energy lattice Boltzmann method[J]. *Meccanica* **2021**, *56* (12), 2961−2977.
(26) Raiskinmäki, P.; Shakib-Manesh, A.; Jäsberg, A.; Koponen, A.; Merikoski, J.; Timonen, J. Lattice-Boltzmann simulation of capillary rise dynamics[J]. *Journal of statistical physics* **2002**, *107*, 143−158.
(27) Wolf, F. G.; dos Santos, L. O. E.; Philippi, P. C. Capillary rise between parallel plates under dynamic conditions [J]. *J. Colloid Interface Sci.* **2010**, *344* (1), 171−179.
(28) Lu, G.; Wang, X. D.; Duan, Y. Y. Study on initial stage of capillary rise dynamics [J]. *Colloids Surf., A* **2013**, *433*, 95−103.
(29) Wang, D.; Liu, P.; Wang, J.; Bao, X.; Chu, H. Direct Numerical Simulation of Capillary Rise in Microtubes with Different Cross-Sections [J]. *Acta Phys. Polonica, A* **2019**, *135* (3), 532.
(30) Cheng, Z.; Ning, Z.; Yu, X.; Wang, Q.; Zhang, W. New insights into spontaneous imbibition in tight oil sandstones with NMR [J]. *J. Pet. Sci. Eng.* **2019**, *179*, 455−464.
(31) Schmid, S. K.; Alyafei, N.; Geiger, S.; Blunt, M. J. Analytical solutions for spontaneous imbibition: fractional flow theory and experimental analysis [J]. *SPE Journal* **2016**, *21* (6), 2308−2316.
(32) Shan, X.; Chen, H. Lattice Boltzmann model for simulating flows with multiple phases and components [J]. *Phys. Rev. E* **1993**, *47* (3), 1815.
(33) Gong, S.; Cheng, P. Numerical investigation of droplet motion and coalescence by an improved lattice Boltzmann model for phase transitions and multiphase flows [J]. *Comput. Fluids* **2012**, *53*, 93−104.
(34) Mukherjee, A.; Basu, D. N.; Mondal, P. K. Algorithmic augmentation in the pseudopotential-based lattice Boltzmann method for simulating the pool boiling phenomenon with high-density ratio [J]. *Phys. Rev. E* **2021**, *103* (5), No. 053302.
(35) Li, Q.; Luo, K. H.; Kang, Q. J.; Chen, Q. Contact angles in the pseudopotential lattice Boltzmann modeling of wetting [J]. *Phys. Rev. E* **2014**, *90* (5), No. 053301.
(36) Yuan, P.; Schaefer, L. Equations of state in a lattice Boltzmann model [J]. *Phys. Fluids* **2006**, *18* (4), No. 042101.
(37) Kupershtokh, A. L.; Medvedev, D. A.; Karpov, D. I. On equations of state in a lattice Boltzmann method [J]. *Computers & Mathematics with Applications* **2009**, *58* (5), 965−974.

(38) Valvatne, P. H.. *Predictive pore-scale modelling of multiphase flow*. Department of Earth Science and Engineering: [D] Imperial College London. 2004.
(39) Huang, H.; Krafczyk, M.; Lu, X. Forcing term in single-phase and Shan-Chen-type multiphase lattice Boltzmann models [J]. *Phys. Rev. E* **2011**, *84* (4), No. 046710.
(40) Wen, B.; Huang, B.; Qin, Z.; Wang, C.; Zhang, C. Contact angle measurement in lattice Boltzmann method [J]. *Comput. Math. App.* **2018**, *76* (7), 1686−1698.
(41) Zhang, T.; Javadpour, F.; Li, J.; Zhao, Y.; Zhang, L.; Li, X. Pore-scale perspective of gas/water two-phase flow in shale [J]. *SPE J.* **2021**, *26* (2), 828−846.
(42) Cheng, Z.; Zhang, W.; Ning, Z.; Dou, L.; Zhan, J.; Zhao, C. Wettability control on imbibition behavior of oil and water in porous media [J]. *Phys. Fluids* **2022**, *34* (7), No. 076603.
(43) Shi, H.; Zhu, Q.; Chen, Z.; Li, J.; Feng, D.; Zhang, S.; Ye, J.; Wu, K. Pore-scale modeling of water−gas flow in heterogeneous porous media [J]. *Phys. Fluids* **2023**, *35* (7), No. 072114.
(44) YUE, P. E. N. G. T. A. O.; FENG, J. J.; LIU, C. H. U. N.; SHEN, J. I. E. A diffuse-interface method for simulating two-phase flows of complex fluids[J]. *J. Fluid Mech.* **2004**, *515*, 293−317.
(45) Cheng, Z.; Gao, H.; Tong, S.; Zhang, W.; Ning, Z. Pore scale insights into the role of inertial effect during the two-phase forced imbibition[J]. *Chem. Eng. Sci.* **2023**, *278*, 118921−118921.
(46) Wylie, Stroberg; Sinan, Keten; Kam, Liu Wing Hydrodynamics of capillary imbibition under nanoconfinement [J]. *Langmuir* **2012**, *28* (40), 14488−14495.
(47) Li, Q.; Luo, K. H. Achieving tunable surface tension in the pseudopotential lattice Boltzmann modeling of multiphase flows [J]. *Phys. Rev. E* **2013**, *88* (5), No. 0533.

https://doi.org/10.1021/acsomega.4c10365
ACS Omega 2025, 10, 3116−3127